Slow and fast topological dynamical phase transitions in a Duffing resonator driven by two detuned tones

Letizia Catalini,[1,2,3,*] Javier del Pino,[4] Soumya S. Kumar,[4] Vincent Dumont,[1,2] Gabriel Margiani,[1,2] Oded Zilberberg,[4] and Alexander Eichler[1,2]

[1]Laboratory for Solid State Physics, ETH Zürich, 8093 Zürich, Switzerland
[2]Quantum Center, ETH Zürich, 8093 Zürich, Switzerland
[3]Center for Nanophotonics, AMOLF, 1098XG Amsterdam, The Netherlands
[4]Department of Physics, University of Konstanz, 78464 Konstanz, Germany

(Received 17 December 2024; accepted 8 June 2025; published 14 July 2025)

Nonlinear dynamics are studied in diverse fields as climate models, avalanches, nanomechanical sensors, optical frequency converters, and electrical quantum amplifiers. A widely studied nonlinear model is the so-called Duffing (or Kerr) resonator, which features a quartic potential term. Two hallmark properties of this model are (i) a shift of a system's resonance frequency as a function of the driving strength, and (ii) monostable or bistable responses, depending on the drive strength and detuning from resonance. Together, these two properties can lead to dynamical phase transitions when several drives are applied simultaneously. Here, we report an experimental and theoretical study of a driven-dissipative nonlinear system with two detuned drives. We observe distinct response regimes characterized by the system's ability to follow the system's time-dependent vector-flow topology. Our work provides an example for understanding dynamical phase transitions in out-of-equilibrium nonlinear systems.

DOI: 10.1103/y9gq-yjxy

I. INTRODUCTION

Measuring the response of a system to a strong "pump" by means of a weak "probe" has been a cornerstone of optical spectroscopy and microscopy for many years [1–4]. In Josephson superconducting circuits, pump-probe measurements are exploited for mode tuning via the AC stark shift [5,6] and to engineer level attraction between signal and idler [7]. In nanomechanics, it is used to investigate the coupling between vibrational modes [8–10], study isolating electronic states in carbon nanotubes [11], and quantify the phase noise squeezing of a resonator [12]. In all these experiments, the probe amplitude is kept small to only explore linear perturbations of the system around the dominant pump-driven physics [13]. This condition separates the impact of the pump tone that sets the stationary state from the probe that induces small fluctuations, making the method versatile and simple to interpret.

While useful for linear systems, the separation of the driving tones into so-called pump and probe severely restricts applications in nonlinear systems to the domain of linear fluctuations around the stationary states of the pump. Away from this linear approximation, the combination of both tones may lead to significant effects that cannot be analyzed separately [7,8,10,14–18]. Essentially, nonlinear dynamics map to vector flows whose topology encode the structural arrangement of attractors and separatrices [19]. These vector flows will dynamically evolve due to the combined tones. Examples where the interplay of the nonlinearity with multiple driving tones leads to new phenomena are strong optomechanical squeezing [20,21], pulse-width modulation [22], parametric symmetry breaking [23], and routes into chaos [24–29]. In the latter two examples, the second tone drives instabilities in the system, leading to new dynamics that are challenging to describe analytically [26,30,31]. In such a setting, the timescale of the beating between the drives relative to relaxation times in the system plays a crucial role in the resulting dynamics.

In this work, we explore the interplay between vector flow and dynamical phase transitions in a single Duffing (Kerr) resonator subject to a combination of two near-resonant drive tones. We measure the response of the resonator by varying the relative strength and detuning of the one of the tones. Under particular conditions, the system response to the two drive tones is characterized by periodic orbits in phase space around the stationary states of the nonlinear resonator. These orbits arise from an interplay between the detuning between the two drives, multistability, and dissipation. We find two separate regimes of orbits, originating from either slow or fast changes in the vector flow relative to the decay time. We explain both regimes with a modified model of the Duffing resonator. Our results thus highlight a key distinction in multitone measurements, and lay the groundwork for future explorations of nonlinear networks. Such networks have important implications for society as model systems to study tipping points in

*Contact author: l.catalini@amolf.nl

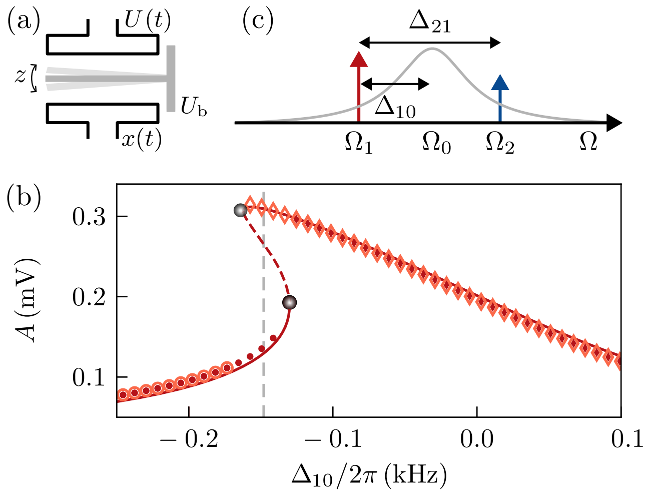

FIG. 1. Experimental setup. (a) Simplified sketch of the tuning fork resonator (light gray) vibrating with displacement $z(t)$ in response to a voltage signal $U(t)$. The capacitive coupling to the lower electrode converts the vibration into an electrical signal $x(t)$. The tuning fork is biased with a voltage $U_b = 32$ V. (b) Measured amplitude response A to a single driving tone $U = 140$ mV swept from low to high (high to low) frequency Ω_1 as filled (empty) blue symbols, with $\Delta_{10} = \Omega_1 - \Omega_0$. Disks and diamonds represent the lower and upper stable solution, respectively. The red solid (dashed) lines represent the analytical stationary stable (unstable) solutions, cf. Eq. (2). Gray spheres highlight the positions of the bifurcation points, cf. Eq. (4), and the gray vertical line corresponds to the tone frequency $\Delta_{10}/2\pi = -148$ Hz used in Fig. 2. (c) In Figs. 2–4, we use a second tone at frequency Ω_2, detuned from the first tone by $\Delta_{21} = \Omega_2 - \Omega_1$.

early warning theories [26,32–34] that pertain, for example, to climate models, avalanches, and economy.

II. EXPERIMENTAL RESULTS

Our experimental setup consists of a double ended tuning fork resonator, made out of single-crystal silicon, which is capacitively coupled to electrodes fabricated next to it [35]; see Fig. 1(a) and [36] for additional details. We employ the lowest mechanical mode, whose resonance frequency Ω_0 and Duffing nonlinearity β is tuned by applying a bias voltage U_b. An oscillating voltage $U(t)$ results in a drive. The resulting displacement $z(t)$ is converted into an oscillating electrical voltage $x(t)$. For simplicity, we treat x as our effective degree of freedom and express all parameters accordingly as those of an effective electrical resonator. Under a strong drive, the response of the system is distinctly nonlinear and can be described by the equation of motion:

$$\ddot{x} + \Omega_0^2 x + \Gamma\dot{x} + \beta x^3 = F(t)\,, \tag{1}$$

with Γ the damping rate, $F(t) = U(t) \times K$ the overall applied drive in units of $\mathrm{V/s^2}$ with a conversion factor $K \approx 1 \times 10^7\,/\,\mathrm{s^2}$, and β the negative (softening) Duffing coefficient. Equation (1) does not contain a term proportional to x^2, as this merely leads to a modified effective value of β, see Chapter 2 in Ref. [37]. In our treatment, this modification is included in the usual calibration of β, and the small effect of pulling due to $\langle F^2\rangle$ is ignored. From calibration measurements, we obtain the parameters $\Omega_0/2\pi = 1.109$ MHz, $\Gamma/2\pi = 110$ Hz, and $\beta = -1.89 \times 10^{17}\,\mathrm{V^{-2}s^{-2}}$ [36].

To characterize our system, we first measure the response of the resonator to a single drive $F(t) = F_1\cos(\Omega_1 t + \theta_1)$ with frequency $\Omega_1 \approx \Omega_0$, fixed phase θ_1, and strength $F_1/K = 140$ mV. We generate the oscillating drive and collect data with a lock-in amplifier [38] set to a local oscillator frequency Ω_1, enabling the down conversion to extract the in-phase (X) and out-of-phase (Y) quadratures defined by $x(t) = X(t)\cos(\Omega_1 t) - Y(t)\sin(\Omega_1 t)$. In Fig. 1(b), we show the measured amplitude response at frequency Ω_1, $A(t) = \sqrt{X(t)^2 + Y(t)^2}$, for sweeps from low to high (high to low) frequencies as filled (empty) dots. In each sweep, we observe a jump between high and low amplitudes, as expected in a Duffing resonator, reflecting transitions between stationary oscillating solutions at the driving frequency Ω_1. The jump position is hysteretic and is influenced by initial conditions and sweep direction.

Next, we add a second weak probe tone, such that $F(t) = \sum_{m=1,2} F_m\cos(\Omega_m t + \theta_m)$. We initialize the system in the low-amplitude stationary solution in Fig. 1(b) at a detuning $\Delta_{10} = \Omega_1 - \Omega_0$, cf. Fig. 1(c). The second tone has an amplitude $F_2 = hF_1$, and a frequency Ω_2 detuned from Ω_1 by $\Delta_{21} = \Omega_2 - \Omega_1$. For $\Delta_{10}/2\pi = -148$ Hz, $h = 0.14$, and $\Delta_{21} \approx 0.09\Gamma$, the response at Ω_1 shows small oscillations around the initial solution (red line and symbols in Fig. 2) with frequency Δ_{21}, see left panel in Fig. 2(a). In the frame rotating at Ω_1, spanned by X and Y, this oscillation forms a closed loop around the initial state, see right panel. Increasing the probe amplitude to $h = 0.21$, we observe a striking change in the response: as shown in Fig. 2(b), the system exhibits large amplitude variations, with X and Y tracing an eight-shaped trajectory which circles the two stable solutions the system has when driven only by F_1 ($h = 0$). Increasing the detuning Δ_{21} while keeping $h = 0.21$ alters the response once more, see Fig. 2(c). Here, the system's quadratures oscillate again around the low-amplitude solution. However, as is discussed below, this case differs from the similar phenomenon in Fig. 2(a), marking a third regime with unique features.

III. EFFECTIVE MODEL

To better understand the differences between the three cases, we write Eq. (1) in the rotating frame measured by the lock-in amplifier at the frequency of the first drive. Assuming the quadratures $X(t), Y(t)$ to vary slowly relative to the drive frequency Ω_1, we average them over the oscillation period $2\pi/\Omega_1$ [30,37]. This yields

$$\begin{aligned}\dot{X} &= -\Gamma\frac{X}{2} - \frac{Y}{2}\left(\frac{3\beta}{4\Omega_1}A^2 + \frac{\Omega_0^2 - \Omega_1^2}{\Omega_1}\right) + \frac{\mathrm{Im}(f(t))}{2\Omega_1},\\ \dot{Y} &= -\Gamma\frac{Y}{2} + \frac{X}{2}\left(\frac{3\beta}{4\Omega_1}A^2 + \frac{\Omega_0^2 - \Omega_1^2}{\Omega_1}\right) - \frac{\mathrm{Re}(f(t))}{2\Omega_1},\end{aligned} \tag{2}$$

with $f(t) = F_1 e^{i\theta_1} + F_2 e^{i(\varphi(t)+\theta_2)}$ and $\varphi(t) = \Delta_{21}t$. For Eq. (2) to hold, $|\beta|A^2/(\Omega_1^2)$, $|\Omega_1^2 - \Omega_0^2|/\Omega_1^2$, and $\sqrt{|\beta|F_m^2/\Omega_1^6}$ must be $\ll 1$ [37]—conditions always fulfilled by our experimental parameters. Equation (2) is valid when the variation of $f(t)$, driven by the detuned second drive and its relative phase $\varphi(t)$,

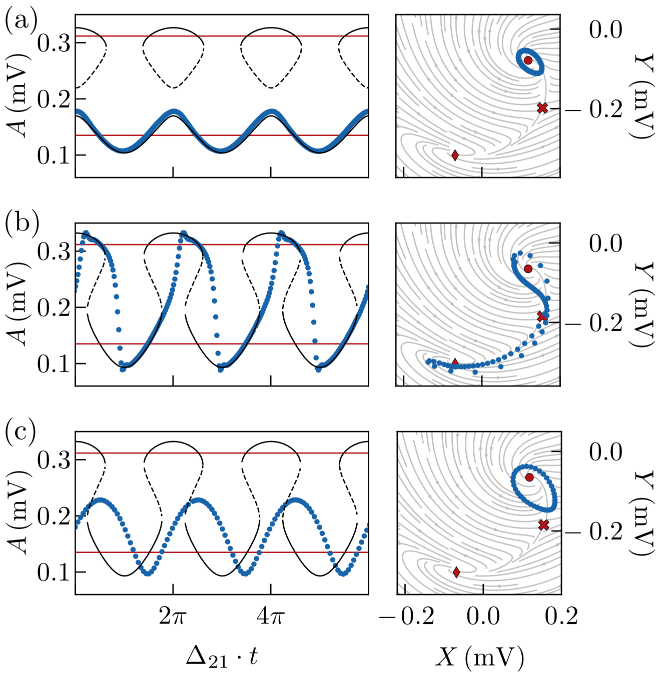

FIG. 2. System response to a two-tone drive. Measured amplitude $A(t)$ over time (left panel) and trajectory in phase space (right panel) for (a) $h \equiv F_2/F_1 = 0.14$ and $\Delta_{21}/2\pi = 10\,\mathrm{Hz}$, (b) $h = 0.21$ and $\Delta_{21}/2\pi = 10\,\mathrm{Hz}$, and (c) $h = 0.21$ and $\Delta_{21}/2\pi = 90\,\mathrm{Hz}$. We initialize the system in the low-amplitude state with a fixed voltage $F_1/K = 140\,\mathrm{mV}$ and $\Delta_{10}/2\pi \approx -148\,\mathrm{Hz}$, cf. Fig. 1(b). Blue points are measured data. On the left, the dark solid (dashed) line represents the calculated time-dependent stable (unstable) stationary solutions, while the red lines indicate the analytical single-tone stationary solutions of the system for $h = 0$ in Eq. (2). On the right, the disk (diamond) represents the low (high) amplitude stable state, corresponding to the red lines on the left. The cross marks the unstable state, and gray lines show the vector flow arising from Eq. (2) for $h = 0$.

is sufficiently slow. The averaging is carried out to second order, introducing a small correction from residual quadratic nonlinearities [additional terms $\propto x^2$ in Eq. (1)], that renormalizes the effective Duffing nonlinearity [37]; this corrected β is the one extracted from the experiment [36].

Intuitively, we can understand the main effect of the two detuned drives as a single amplitude-modulated drive with

$$|f(t)| = F_1\sqrt{1 + h^2 + 2h\cos(\theta_1 - \theta_2 - \varphi(t))}\,. \tag{3}$$

Within each period $1/\Delta_{12}$, the resonator experiences a drive amplitude ranging from $F_1 - F_2$ (drives are completely out of phase) to $F_1 + F_2$ (drives are in phase). For an effective drive f at a single point in time, we can set $\dot{X} = \dot{Y} = 0$ in Eq. (2) and obtain either one or two stable stationary solutions at frequency Ω_1 [30,37]. For $h = 0$, this yields the stationary amplitudes and bifurcations of the single-tone Duffing resonator; see Fig. 1(b) [36]. The bifurcation points occur when

$$|f|^2 = \frac{8}{81\beta}\left[\left(\tilde{\Delta}_{01}^4 - 3\Gamma^2\Omega_1^2\right)^{\frac{3}{2}} \pm \tilde{\Delta}_{01}^2\left(\tilde{\Delta}_{01}^4 + 9\Gamma^2\Omega_1^2\right)\right], \tag{4}$$

with $\tilde{\Delta}_{01} = \sqrt{\Omega_0^2 - \Omega_1^2}$ [36]. The effective drive f therefore sets the position of the two bifurcation frequencies. Since the

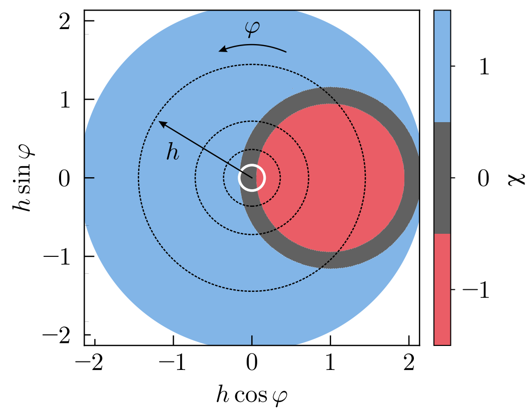

FIG. 3. Calculated topological phase diagram for the two-tone driven Duffing resonator. We use $F_1/K = 140\,\mathrm{mV}$ and $\Delta_{10}/2\pi \approx -148\,\mathrm{Hz}$ as in Fig. 2. Depending on the amplitude $h = F_2/F_1$ and the phase φ between the drives [cf. Eq. (3)], the system can have a net chirality $\chi = 1$, 0, or -1, corresponding to distinct topological phases that offer only the high-amplitude solution (monostable), both solutions (bistable), or only the low-amplitude solution (monostable), respectively. The white ring represents the critical value of h to enter the high-amplitude monostable region.

drive is amplitude modulated, the detunings Δ_{10} at which the bifurcation points occur are also modulated, cf. Eq. (4). If the modulation is strong enough, the number of stable solutions at Ω_1 changes between 1 and 2 periodically.

Note that Eq. (2) defines a 2D vector flow, shown as gray lines in the phase space graphs in Fig. 2. Different solutions of the system are characterized by different flow chiralities, where we assign the value 1 (-1) to a clockwise (counterclockwise) chirality, highlighting whether the dynamics is advanced or delayed relative to the driving tone. In the Duffing resonator with $\beta < 0$, the upper (lower) solution has a chirality of 1 (-1) [39–41]. We can solve for all stable stationary solutions $i \in \{1, 2\}$ as a function of $h\cos\varphi$ and $h\sin\varphi$, and at each point sum over their chiralities χ_i, see Fig. 3. This yields a net chirality $\chi = \sum_i \chi_i$. When the low-and high-amplitude solutions coexist, $\chi = 0$. The net chirality is a sufficient topological index for our system [19]. To summarize, structural changes in the vector flow manifest as changes in the number of solutions and their local flow chirality, indicating topological phase transitions.

We return now to our two-tone dynamical system. For a fixed second drive with relative amplitude $h > 0$, the system traverses a circular path in the stationary phase diagram [Fig. 3] as its phase φ evolves over time. The path can traverse regions with different χ and may induce dynamical phase transitions [42] between low- and high-amplitude solutions. Nonetheless, the system's ability to undergo a dynamical phase transition and reach the vicinity of a new solution depends on the available time before the solution vanishes again. To determine which solutions are reached over time in the experiment, we track the stationary amplitudes along each circular trajectory in Fig. 3 and overlay them with the observed $A(t)$ in the left panels of Fig. 2. When the drive modulation is relatively small ($h = 0.14$), the low-amplitude solution never loses stability, and the system remains trapped near the initial single-tone solution; see Fig. 2(a). In contrast, the case with an

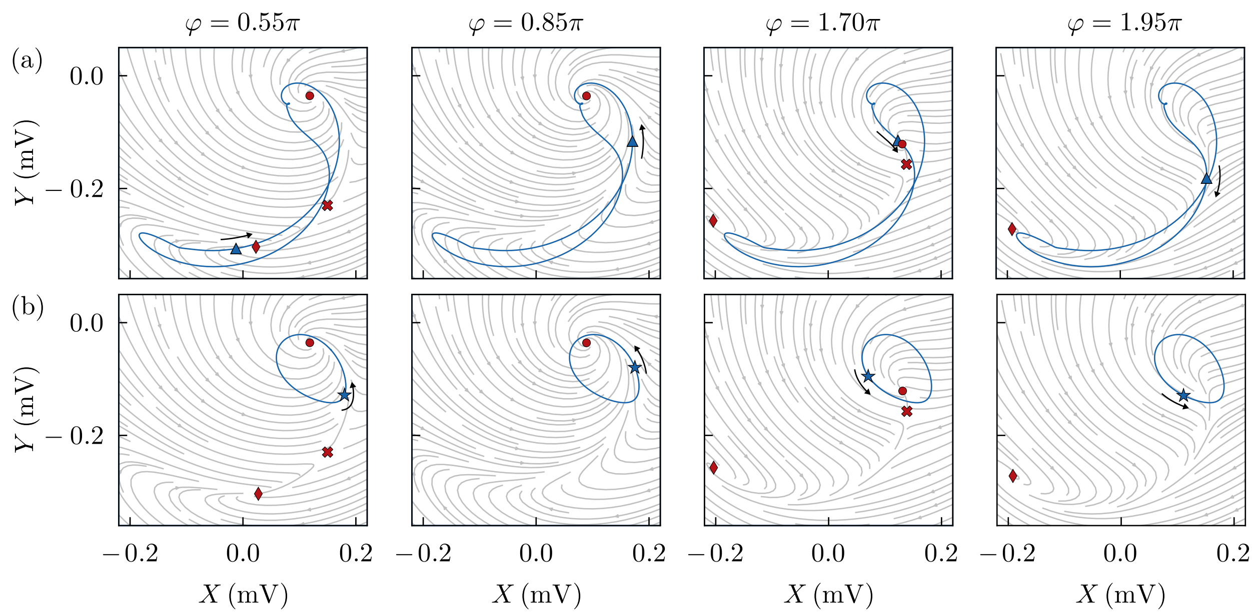

FIG. 4. Simulated qualitative difference between the slow and fast regime. (a) From left to right we show snapshots at various φ (top labels) during a single modulation cycle of the slow ($\Delta_{21}/2\pi = 10\,\mathrm{Hz}$) regime. The instantaneous solution (blue triangle) initially continuously follows the high amplitude solution (red diamond), jumps to the low-amplitude solution (red disk), continuously follows the low-amplitude solution, and then jumps to the high-amplitude solution. (b) Same snapshots in the fast ($\Delta_{21}/2\pi = 90\,\mathrm{Hz}$) regime. Here, in contrast, the instantaneous solution (blue star) remains confined to a trajectory around the low-amplitude solution. Parameters are the same as in the corresponding experiments in Fig. 2, with $\varphi = \Delta_{21}t$. The analytically calculated positions of the two stable (red disk and diamond) and the unstable solution (red cross), as well as the instantaneous system position, are shown together with a numerical simulation of the entire trajectory (blue line). Gray lines represent the stationary vector flow calculated from Eq. (2) assuming an effective instantaneous force f [Eq. (3)] with $h = 0.21$ and a different phase φ in each panel (top labels).

increased probe strength ($h = 0.21$) in Fig. 2(b) corresponds to a trajectory in Fig. 3 that enters both the low-amplitude monostable region (red) and the high-amplitude monostable region (blue). The system follows stable solutions until they vanish at a bifurcation point, forcing a periodic jump between low- and high-amplitude Duffing solutions. This corresponds to repeated dynamical phase transition imposed periodically by $\varphi(t)$. As the system has enough time to probe the change in topology, we term this regime "slow."

The slow regime ($\Delta_{2,1} < \Gamma$), which we explore in Fig. 2(b), was also studied in Ref. [22]. It can be compared to an hourglass where all the sand collects on the lower side before being turned. Such phenomena are studied in a broad range of fields, ranging from bursting oscillations observed in nonlinear coupled systems [43] to tipping points of avalanches [26,44]. By contrast, in Fig. 2(c), we used $\Delta_{21} \approx \Gamma$. Even though the stationary solutions and chiralities are identical to the ones in Fig. 2(b) and we follow the same path in Fig. 3, the system cannot probe the changing vector-flow topology quickly enough. The jumps are thus never completed, and the system orbits around the initial single-tone solution. To distinguish from the slow case above, we term this regime "fast." The fast case contrasts with Fig. 2(a), where the system can follow a single stationary state continuously because that solution remains available during the entire period.

To emphasize the difference between the slow regime in Fig. 2(b) and the fast regime in Fig. 2(c), Fig. 4 presents snapshots of the accumulated system's trajectory at different times during a single period, shown alongside the instantaneous vector flow. The vector flow lines are calculated using Eq. (2), with the same parameters as in Figs. 2(b) and 2(c). A numerical simulation of the slow regime is shown in Fig. 4(a). Like in the experiment in Fig. 2(b), we observe the characteristic eight-shaped trajectory due to the opposite chirality of the flow lines around the two solutions. In the fast regime in Fig. 4(b), instead, the simulated trajectory is strikingly different, even though the global topology of the flow lines is identical. Here, the system is trailing (but never quite catching up with) the low-amplitude solution or the changing topology of the flow lines. The resulting small loop strongly resembles the experimental observation in Fig. 2(c). The time-dependent flow analysis thus reveals stark contrast between the slow and fast regimes, driven by the interplay of modulation timescales and dissipation, and traceable to the system's capacity—or lack thereof—to adapt to changing conditions. Interestingly, a systematic study of the system response to various Δ_{12} and h reveals a nontrivial transition between fast and slow regimes; see Sect. III of [36]. We leave the analytical description of such interplay to future work.

IV. CONCLUSION AND OUTLOOK

This work exemplifies the competition between an amplitude-modulated drive and resonator damping in a nonlinear oscillator. In particular, we highlight the transition from a slow regime, where the system adheres to the underlying topology of the phase-space dynamics and undergoes dynamical phase transitions, to a fast regime where this is no longer true. While starting from a similar situation as previous works [24–29], we thus emphasize a fundamental aspect that was hitherto not well addressed: why does the system select a particular trajectory in response to multitone drives, and how can it be controlled? The insights from this example are broadly applicable to other nonlinear systems, particularly to networks of nonlinear resonators, where the coupling terms of the individual network constituents act as multiple drive tones that can induce many-body oscillation phases [45–48]. Characterizing these phases in terms of their time-dependent phase-space topology [19] and departures therefore will provide a robust framework for sensing applications [22], computer vision [49], and kinematic synthesis in complex machinery [50], as well as further our understanding of water wave dynamics [51,52] and combustion engines [53], as well as early-warning models [26] employed in the context of avalanches, earthquakes, and solar flares [44].

ACKNOWLEDGMENTS

The authors acknowledge Christian Marti and Sebastián Guerrero for help building the measurement setup. We thank Nicholas E. Bousse and T. W. Kenny for providing the MEMS device, and Joel Moser for inspiring discussions. V.D. acknowledges support from the ETH Zurich Postdoctoral Fellowship Grant No. 23-1 FEL-023. O.Z. acknowledges funding from the Deutsche Forschungsgemeinschaft (DFG) via Project No. 449653034 and through SFB1432. A.E. and O.Z. acknowledge financial support from the Swiss National Science Foundation (SNSF) through the Sinergia Grant No. CRSII5_206008/1.

DATA AVAILABILITY

The data that support the findings of this article are openly available [54].

[1] A. Owyoung, Coherent raman gain spectroscopy using CW laser sources, IEEE J. Quantum Electron. **14**, 192 (1978).

[2] F. E. Lytle, R. M. Parrish, and W. T. Barnes, An introduction to time-resolved pump/probe spectroscopy, Appl. Spectrosc. **39**, 444 (1985).

[3] J. W. R. Tabosa, G. Chen, Z. Hu, R. B. Lee, and H. J. Kimble, Nonlinear spectroscopy of cold atoms in a spontaneous-force optical trap, Phys. Rev. Lett. **66**, 3245 (1991).

[4] S. Mukamel, *Principles of Nonlinear Optical Spectroscopy*, Oxford Series in Optical and Imaging Sciences (Oxford University Press, New York, 1995).

[5] Y. Chu, P. Kharel, W. H. Renninger, L. D. Burkhart, L. Frunzio, P. T. Rakich, and R. J. Schoelkopf, Quantum acoustics with superconducting qubits, Science **358**, 199 (2017).

[6] U. von Lüpke, Y. Yang, M. Bild, L. Michaud, M. Fadel, and Y. Chu, Parity measurement in the strong dispersive regime of circuit quantum acoustodynamics, Nat. Phys. **18**, 794 (2022).

[7] F. Fani Sani, I. C. Rodrigues, D. Bothner, and G. A. Steele, Level attraction and idler resonance in a strongly driven josephson cavity, Phys. Rev. Res. **3**, 043111 (2021).

[8] H. J. R. Westra, M. Poot, H. S. J. van der Zant, and W. J. Venstra, Nonlinear modal interactions in clamped-clamped mechanical resonators, Phys. Rev. Lett. **105**, 117205 (2010).

[9] A. Eichler, M. del Álamo Ruiz, J. A. Plaza, and A. Bachtold, Strong coupling between mechanical modes in a nanotube resonator, Phys. Rev. Lett. **109**, 025503 (2012).

[10] T. Antoni, K. Makles, R. Braive, T. Briant, P.-F. Cohadon, I. Sagnes, I. Robert-Philip, and A. Heidmann, Nonlinear mechanics with suspended nanomembranes, Europhys. Lett. **100**, 68005 (2012).

[11] I. Khivrich, A. A. Clerk, and S. Ilani, Nanomechanical pump–probe measurements of insulating electronic states in a carbon nanotube, Nat. Nanotechnol. **14**, 161 (2019).

[12] J. S. Ochs, M. Seitner, M. I. Dykman, and E. M. Weig, Amplification and spectral evidence of squeezing in the response of a strongly driven nanoresonator to a probe field, Phys. Rev. A **103**, 013506 (2021).

[13] G. Khitrova, P. R. Berman, and M. Sargent, Theory of pump–probe spectroscopy, J. Opt. Soc. Am. B **5**, 160 (1988).

[14] R. W. Boyd and S. Mukamel, Origin of spectral holes in pump-probe studies of homogeneously broadened lines, Phys. Rev. A **29**, 1973 (1984).

[15] J. H. Eberly and V. D. Popov, Phase-dependent pump-probe line-shape formulas, Phys. Rev. A **37**, 2012 (1988).

[16] E. Gaižauskas and L. Valkūnas, Coherent transients of pump-probe spectroscopy in two-level approximation, Opt. Commun. **109**, 75 (1994).

[17] V. Bonačić-Koutecký and R. Mitrić, Theoretical exploration of ultrafast dynamics in atomic clusters: Analysis and control, Chem. Rev. **105**, 11 (2005).

[18] M. Frimmer, T. L. Heugel, Ž. Nosan, F. Tebbenjohanns, D. Hälg, A. Akin, C. L. Degen, L. Novotny, R. Chitra, O. Zilberberg, and A. Eichler, Rapid flipping of parametric phase states, Phys. Rev. Lett. **123**, 254102 (2019).

[19] G. Villa, J. del Pino, V. Dumont, G. Rastelli, M. Michałek, A. Eichler, and O. Zilberberg, Topological classification of driven-dissipative nonlinear systems, arXiv:2406.16591.

[20] A. Kronwald, F. Marquardt, and A. A. Clerk, Arbitrarily large steady-state bosonic squeezing via dissipation, Phys. Rev. A **88**, 063833 (2013).

[21] W. Zhang, T. Wang, X. Han, S. Zhang, and H.-F. Wang, Mechanical squeezing induced by duffing nonlinearity and two driving tones in an optomechanical system, Phys. Lett. A **424**, 127824 (2022).

[22] S. Houri, R. Ohta, M. Asano, Y. M. Blanter, and H. Yamaguchi, Pulse-width modulated oscillations in a nonlinear resonator under two-tone driving as a means for mems sensor readout, Jpn. J. Appl. Phys. **58**, SBBI05 (2019).

[23] A. Leuch, L. Papariello, O. Zilberberg, C. L. Degen, R. Chitra, and A. Eichler, Parametric symmetry breaking in a nonlinear resonator, Phys. Rev. Lett. **117**, 214101 (2016).

[24] K. Ide and S. Wiggins, The bifurcation to homoclinic tori in the quasiperiodically forced duffing oscillator, Physica D **34**, 169 (1989).

[25] A. Belogortsev, Bifurcations of tori and chaos in the quasiperiodically forced duffing oscillator, Nonlinearity **5**, 889 (1992).

[26] S. Strogatz, *Nonlinear Dynamics and Chaos: With Applications to Physics, Biology, Chemistry, and Engineering*, repr. ed., Studies in Nonlinearity (Westview Press, Cambridge, Mass, 2007).

[27] S. Houri, M. Asano, H. Yamaguchi, N. Yoshimura, Y. Koike, and L. Minati, Generic rotating-frame-based approach to chaos generation in nonlinear micro- and nanoelectromechanical system resonators, Phys. Rev. Lett. **125**, 174301 (2020).

[28] G. Madiot, F. Correia, S. Barbay, and R. Braive, Bichromatic synchronized chaos in driven coupled electro-optomechanical nanoresonators, Phys. Rev. A **104**, 023525 (2021).

[29] M. Defoort, L. Rufer, L. Fesquet, and S. Basrour, A dynamical approach to generate chaos in a micromechanical resonator, Microsyst. Nanoeng. **7**, 17 (2021).

[30] J. Košata, J. del Pino, T. L. Heugel, and O. Zilberberg, HarmonicBalance.jl: A Julia suite for nonlinear dynamics using harmonic balance, SciPost Phys. Codebases, 6 (2022).

[31] J. del Pino, J. Košata, and O. Zilberberg, Limit cycles as stationary states of an extended harmonic balance ansatz, arXiv:2308.06092.

[32] C. Kuehn, K. Lux, and A. Neamţu, Warning signs for non-markovian bifurcations: colour blindness and scaling laws, Proc. R. Soc. A **478**, 20210740 (2022).

[33] F. Ragone, J. Wouters, and F. Bouchet, Computation of extreme heat waves in climate models using a large deviation algorithm, Proc. Natl. Acad. Sci. USA **115**, 24 (2018).

[34] T. M. Bury, R. I. Sujith, I. Pavithran, M. Scheffer, T. M. Lenton, M. Anand, and C. T. Bauch, Deep learning for early warning signals of tipping points, Proc. Natl. Acad. Sci. USA **118**, e2106140118 (2021).

[35] M. Agarwal, S. A. Chandorkar, H. Mehta, R. N. Candler, B. Kim, M. A. Hopcroft, R. Melamud, C. M. Jha, G. Bahl, G. Yama, T. W. Kenny, and B. Murmann, A study of electrostatic force nonlinearities in resonant microstructures, Appl. Phys. Lett. **92**, 104106 (2008).

[36] See Supplemental Material at http://link.aps.org/supplemental/10.1103/y9gq-yjxy for details on device, characterization, numerical simulation and additional data.

[37] A. Eichler and O. Zilberberg, *Classical and Quantum Parametric Phenomena* (Oxford University Press, Oxford, 2023).

[38] Zurich Instrument MFLI manual.

[39] M. Soriente, R. Chitra, and O. Zilberberg, Distinguishing phases using the dynamical response of driven-dissipative light-matter systems, Phys. Rev. A **101**, 023823 (2020).

[40] M. Soriente, T. L. Heugel, K. Omiya, R. Chitra, and O. Zilberberg, Distinctive class of dissipation-induced phase transitions and their universal characteristics, Phys. Rev. Res. **3**, 023100 (2021).

[41] V. Dumont, M. Bestler, L. Catalini, G. Margiani, O. Zilberberg, and A. Eichler, Energy landscape and flow dynamics measurements of driven-dissipative systems, Phys. Rev. Res. **6**, 043012 (2024).

[42] M. Heyl, A. Polkovnikov, and S. Kehrein, Dynamical quantum phase transitions in the transverse-field ising model, Phys. Rev. Lett. **110**, 135704 (2013).

[43] D. Zhang and Y. Qian, Bursting oscillations in general coupled systems: A review, Mathematics **11**, 1690 (2023).

[44] Z. Ma, C. Zeng, and W.-M. Liu, Relaxation time as early warning signal of avalanches in self-organizing systems, Phys. Rev. Res. **6**, 013013 (2024).

[45] L. Bello, M. Calvanese Strinati, E. G. Dalla Torre, and A. Pe'er, Persistent coherent beating in coupled parametric oscillators, Phys. Rev. Lett. **123**, 083901 (2019).

[46] M. H. Matheny, J. Emenheiser, W. Fon, A. Chapman, A. Salova, M. Rohden, J. Li, M. H. de Badyn, M. Pósfai, L. Duenas-Osorio, M. Mesbahi, J. P. Crutchfield, M. C. Cross, R. M. D'Souza, and M. L. Roukes, Exotic states in a simple network of nanoelectromechanical oscillators, Science **363**, eaav7932 (2019).

[47] T. L. Heugel, M. Oscity, A. Eichler, O. Zilberberg, and R. Chitra, Classical many-body time crystals, Phys. Rev. Lett. **123**, 124301 (2019).

[48] M. P. Zaletel, M. Lukin, C. Monroe, C. Nayak, F. Wilczek, and N. Y. Yao, Colloquium: Quantum and classical discrete time crystals, Rev. Mod. Phys. **95**, 031001 (2023).

[49] R. Hamerly, L. Bernstein, A. Sludds, M. Soljačić, and D. Englund, Large-scale optical neural networks based on photoelectric multiplication, Phys. Rev. X **9**, 021032 (2019).

[50] J. Angeles and S. Bai, *Kinematics of Mechanical Systems: Fundamentals, Analysis and Synthesis*, Mathematical Engineering (Springer, Cham, 2022), pp. XVIII, 329.

[51] F. Simonelli and J. P. Gollub, Surface wave mode interactions: effects of symmetry and degeneracy, J. Fluid Mech. **199**, 471 (1989).

[52] B. Apffel and R. Fleury, Experimental observation of topological transition in linear and nonlinear parametric oscillators, Phys. Rev. E **109**, 054204 (2024).

[53] A. K. Stoychev and N. Noiray, Nonlinear dynamics of an acoustically compact orifice, J. Sound Vib. **593**, 118660 (2024).

[54] L. Catalini, J. del Pino, S. S. Kumar, V. Dumont, G. Margiani, O. Zilberberg, and A. Eichler, Slow and fast topological dynamical phase transitions in a Duffing resonator driven by two detuned tones [Data set], Zenodo (2025), https://doi.org/10.5281/zenodo.15705185.